Available online at www.sciencedirect.com
ScienceDirect
Journal of the European Ceramic Society 28 (2008) 2441–2449
www.elsevier.com/locate/jeurceramsoc

Coordination measurements in compacted NaCl irregular powders using X-ray microtomography

A. Marmottant [a], L. Salvo [a], C.L. Martin [a,*], A. Mortensen [b]

[a] *Laboratoire SIMAP, GPM2 INPGrenoble, UJF-CNRS 101, rue de la physique, BP46 38402 Saint Martin d'Hères cedex, France*
[b] *Laboratoire de métallurgie mécanique, Ecole Polytechnique Fédérale de Lausanne, MX-D Ecublens, CH-015 Lausanne, Switzerland*

Received 29 February 2008; received in revised form 26 March 2008; accepted 27 March 2008
Available online 3 June 2008

Abstract

X-ray microtomography and three-dimensional (3D) image analysis are used to quantify the structural evolution during cold isostatic compaction of two irregularly shaped NaCl powders having different mean particle sizes (75 and 400 μm) and somewhat different aspect ratios. Varying the compaction pressure to vary the powder packing density, the structure of the different packings is quantified in terms of the mean coordination number and of the mean contact area between contacting particles. These parameters are extracted using a 3D image analysis algorithm that is tested beforehand for consistency with compacted monosized sphere packings generated numerically. It is found that the mean area of contact between the irregular particles, which have been studied here, varies, as a function of relative density, according to the same relationship as that derived for spherical particles. The number of contacts, and hence the total contact area, per particle are on the other hand roughly 50% higher than for compacted monomodal spheres.

Keywords: Synchrotron radiation; Particulate material; Compaction

1. Introduction

Because of their ubiquity in industry and in the environment, powders are the subjects of a vast body of research. In ceramic materials engineering notably, powder processes are the main production pathways. These processes are strongly dependent on the geometry of particle compacts and its evolution under the influence of applied pressure and/or at elevated temperature. The physics of powder packing is, therefore, one of the main elements of the science of powder densification processes.[1–7]

In the theory of densification processes, powder particles are generally assimilated to spheres, most often of a single size. For monomodal spherical powders, the coordination number Z and contact area A have been measured using quantitative metallography,[8] and their evolution with the packing density was predicted by Arzt[1,9] whose model was later simplified by Helle et al.[10] Since that time, several other authors have also used micromechanical analysis (e.g., [11]) and experiment (e.g., [12]) to characterize these structural parameters.

Numerical methods have also been used to simulate the cold compaction of monosized particles, notably using the discrete element method (DEM).[13–15] This method considers each particle individually as an autonomous body that moves according to given interaction laws. It enables the computation of relevant structural parameters for each particle, including its position, its coordination number and its contact area with neighbouring particles.

A powerful new tool for the experimental characterization of packed powder compacts is offered by high-resolution X-ray microtomography. For example, the radial density distribution function was computed for sandpile (359 granules) in Ref. 16, a very accurate investigation of a random dense packing containing 380 000 monosized spheres was performed by Aste,[17] and multisized glass sphere packings were investigated for coordination number by Georghalli and Reuter. [18] Some three-dimensional (3D) measurements were also performed on sintered (uncompacted) spherical powders, of glass [19] or copper.[20]

* Corresponding author. Tel.: +33 4 76 82 63 37; fax: +33 4 76 82 63 82.
E-mail address: christophe.martin@simap.grenoble-inp.fr (C.L. Martin).

0955-2219/$ – see front matter © 2008 Elsevier Ltd. All rights reserved.
doi:10.1016/j.jeurceramsoc.2008.03.041

A far smaller body of work has been devoted to the packing of non-spherical particles[4,21,22]; however, these are beginning to be tackled using current modeling methods. 3D packings of prolate and oblate ellipsoids were simulated by Donev et al. and Chaikin et al.[23,24] and the mean coordination number was extracted as a function of the particle aspect ratio. The authors confirmed their results with experiments for one aspect ratio. Several other authors have proposed models tackling non-spherical particle shapes using discrete element models.[15,25–27]

To our knowledge there is little experimental 3D investigation of the influence of compaction on the coordination number and contact area of irregular particles. This is the aim of the investigation reported here: we quantify, using computed microtomography, the structural evolution of sodium chloride particle packings during cold compaction. NaCl powders are used for several reasons. First, sodium chloride powders have an irregular shape: particles exhibit flat facets that are likely to influence their behaviour during packing and compaction. Secondly, NaCl is a good model system for the compaction of ceramic powders. Finally, pressed NaCl powder compacts are used to produce microcellular aluminum by the replication technique.[28,29]

We begin by presenting the experimental methods used. These include the production, the 3D imaging by X-ray tomography and the 3D image analysis methods, including the algorithm that was used to extract quantitative parameters of the irregular packings. We then present numerical simulation results of the random dense packing of monosized spheres. Such numerical packings, obtained with the DEM, have the advantage of possessing topological properties that are easily calculated. As such these offer a discriminating yardstick for the validity of our image analysis algorithm.[30,31] Once validated on numerically simulated sphere packings, we use our 3D image analysis algorithm on experimental tomography data for irregularly shaped NaCl particles. As will be seen, there are differences between irregularly shaped and spherical particle packings but the data suggest that spheres should nonetheless be a good model for the kinetics and mechanics of powder densification.

2. Experimental procedure

2.1. Sample preparation and X-ray microtomography

Two series of sodium chloride powders were used: (i) a "fine" powder with an average particle size close to 75 μm (CP1, Salines de Bex, CH-Bex sieved between 63 and 90 μm meshes), (ii) a "coarse" powder, with an average particle size close to 400 μm (Fluka Chemie GmbH, Buchs Switzerland, sieved with a 250 μm mesh).

Each powder was packed under applied vibration in a cylindrical silicone mould (internal dimensions: 30 mm in diameter, and 110 mm in length) and compacted by cold isostatic pressing. Six pressures were used to produce samples with different packing densities. Small parallelepiped samples were then machined within the resulting salt patterns for X-ray microtomography (1.5 mm^2 section for the 75 μm salt, and 8 mm^2 section for the 400 μm salt).

X-ray microtomography was performed at ESRF (European Synchrotron Radiation Facility, Grenoble, ID 19 beamline), with an optic of 1.9 μm for the fine salt and an optic of 10 μm for the coarser salt and using an energy of 20 keV for both. These experimental conditions lead to a voxel size of 1.9 and 10 μm, respectively. In the process, 900 projections are taken while the sample is rotating over 0–180°. Conventional back projection algorithms are then used to obtain the 3D volume of the sample and images thereof. Finally, 3D image analysis is performed to extract quantitative parameters as a function of the packing density.

2.2. Numerical sphere packings

Monomodal packings of 400–4000 spherical particles are generated numerically in a periodic box using the *dp3D* DEM code.[14,15] We have shown that 400 particles are sufficient to give statistically meaningful results when periodic boundary conditions are used with monomodal packings. Contact forces between neighbouring particles are calculated and mechanical equilibrium of each individual particle is imposed using a dynamic scheme. Contact forces may be elastic or plastic depending on the indentation at the contact and the imposed elastic limit. The procedure for obtaining an initially random jammed packing consists in using a gas of nonoverlapping spheres located at random positions in the periodic box (resulting in a low packing fraction of approximately 0.32). This gas is then submitted to hydrostatic densification and elastic contacts appear between particles. As the densification proceeds, these elastic contacts become more numerous and since the packing become more jammed, the stress at the contacts increases. We have shown that for frictionless particles, and for a realistic elastic limit (here set at 80 MPa), a first plastic contact appears at a packing fraction close to the random close packing fraction of 0.64.[14] We choose this as the initial packing for further plastic compaction.

Cold isostatic compaction of this jammed packing is then simulated, using a zero interparticle friction coefficient. The mean coordination number and the mean contact area are computed directly from the simulation files, knowing the indentation level of the particles and their plastic contact deformation law (perfect plasticity is assumed here).

In order to validate the 3D image analysis developed in this work, the numerical packings are also digitized using a procedure, described in Ref. 32, that generates a file similar to that which the tomograph would generate were it to characterize the simulated structure. The mean coordination number and mean contact area are then measured using 3D image analysis and compared to DEM values (Section 3).

2.3. 3D image analysis

Four parameters are measured on the 3D tomography images, namely: (i) the aspect ratio, (ii) the volume, (iii) the connectivity Z of each particle, and (iv) the mean contact area A between contacting particles. To compute these parameters, it is necessary to clearly distinguish each particle in the packing.[18] This

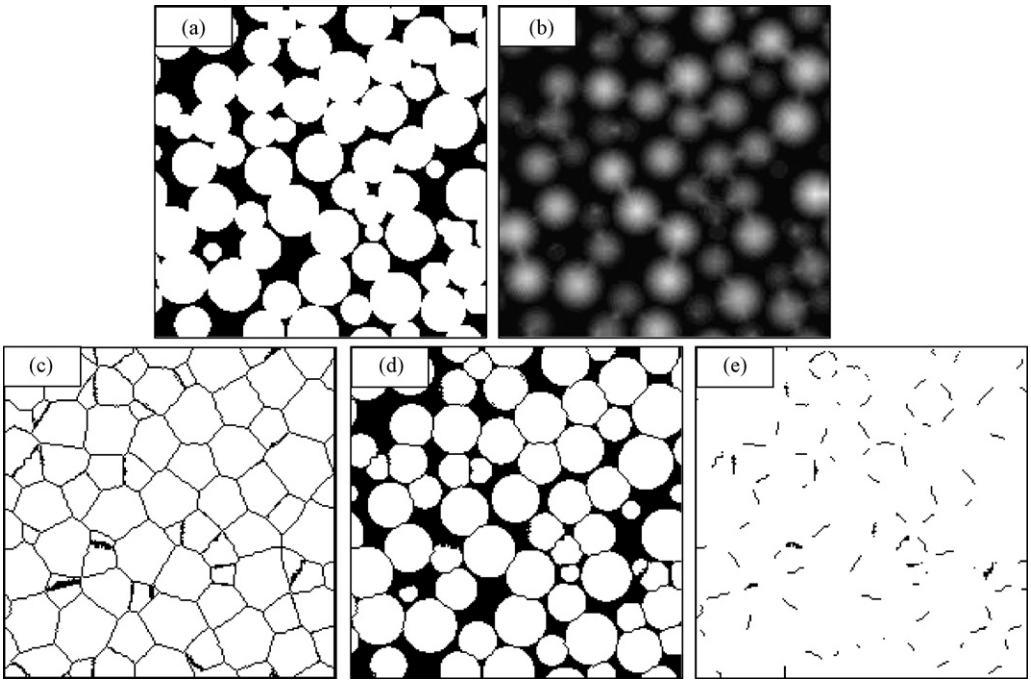

Fig. 1. Method for separating the particles (2D cuts are displayed for sake of clarity but the image treatment is performed in 3D): (a) binarized image (particles are in white), (b) distance map, (c) isolation of the basins, (d) separated particles, and (e) vizualisation of the contacts.

is not a trivial task with the irregularly shaped particles that are studied here. To this end, particles were separated using 3D morphological operations with the Aphelion software (Herouville Saint-Clair, France). Fig. 1 illustrates how this 3D routine proceeds, using two-dimensional (2D) sketches for clarity. A distance map of the initial 3D image is first created: for every "white" (solid) voxel point of the input image a grey level is assigned: its value is the distance to the nearest "black" (void) voxel. This leads to a picture composed of a continuum of grey levels where voxels in each particle are at their lightest at the particle centre and at their darkest on the borders, the regions between the particles being black (Fig. 1(b)). If for visual simplicity we consider this 2D sketch as a topographical relief map where the lightest voxels represent peaks, the black voxels are basins. These basins are then located using a local minima search routine and morphological dilations are performed in order to avoid an excessive number of basins. A conventional 3D watershed routine is then employed,[33] which produces particle surface separation surfaces (lines in a 2D sketch), Fig. 1(c). The intersection of this last image and the initial image leads to a picture with the same particles now separated by a relatively flat surface along their contacts, Fig. 1(d). The difference between Fig. 1(d) and (a) finally allows for a direct visualization of the contacts between the particles, Fig. 1(e).

Once all the particles are separated, each is tagged, i.e., is given a number. Excluding border particles, the volume of each particle is obtained using the marching cubes algorithm.[34] The orientation of each particle is then calculated. Shape information is extracted by identifying the inertia matrix of each particle to that of a parallelepiped of sides having the three length values a, b and c (with $a < b < c$).

The mean coordination number Z within each packing is then computed directly, Fig. 1(e) and (d). The contact area of each particle is obtained through a dilation technique, and the intersection with its contacts is insulated. These contacts are counted, and their surface S is computed using the "marching cubes" algorithm.[34] The real total contact area is then computed as $A = S/2$ (a small error is introduced at the edges due to the finite contact thickness).

For both particle sizes, at least 700 particles were analyzed in order to get meaningful statistical data. Visualizations of a non-compacted packing of 400 μm particles (packing density: 0.68) are given in the form of a two-dimensional cut of the initial packing in Fig. 2(a). The corresponding result of the 3D separation of the irregular particles is presented in Fig. 2(b) and a 3D rendering of the entire packing with separated particles is shown in Fig. 2(c).

3. Validation of the image analysis method: simulated compacted monomodal spheres

Before the present 3D image analysis routine was used on experimental tomography files, it was tested by confrontation with DEM simulation files. Seven 3D sphere packings were thus digitized from the results of the DEM simulations described in Section 2.2, thus creating seven computer-generated 3D image files that were processed using the present image analysis routine. Dimensions of the volumes were 200 voxel × 200 voxel × 200 voxel, and their relative densities ranged from 0.64 to 0.90 depending of the imposed compaction during the DEM simulations. Fig. 3 shows 3D renderings of an initial packing and of two corresponding compacted packings after digitization.

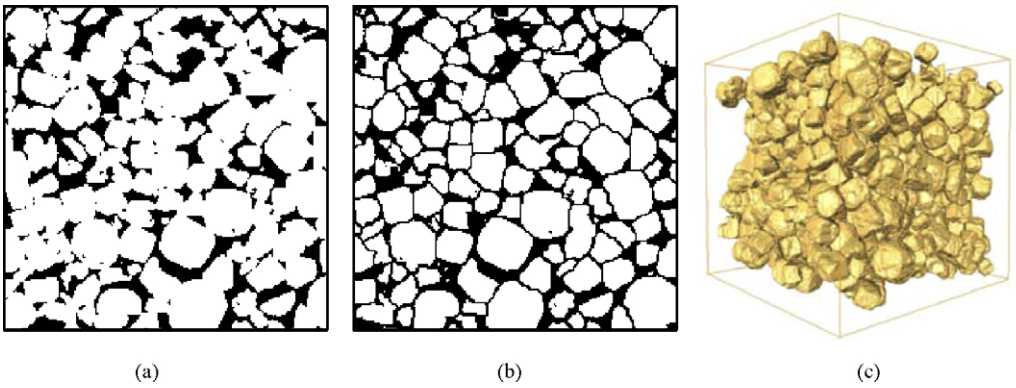

Fig. 2. Initial, as-packed, powder bed structure ($\Delta_E = 0.68$): (a) 2D cut of the initial picture, (b) same after separation; area is about 5 mm^2, and (c) 3D rendering.

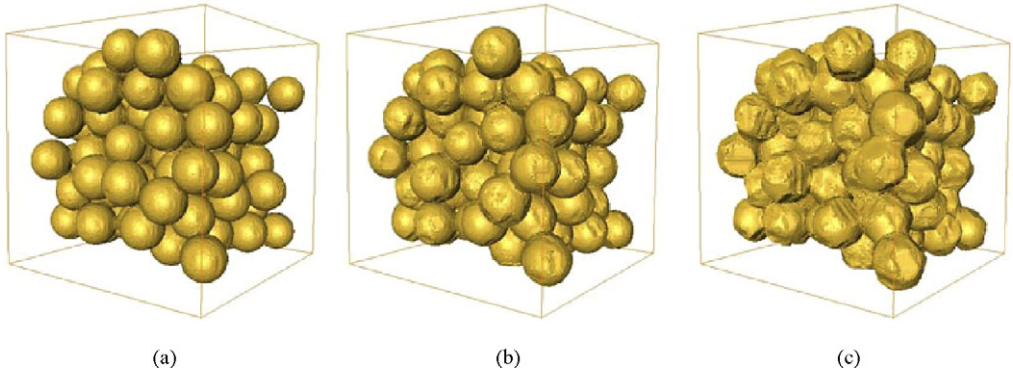

Fig. 3. Example of 3D rendering of digitized compacted sphere packings produced by the discrete element method: (a) $\Delta = 0.64$, (b) $\Delta = 0.76$, and (c) $\Delta = 0.90$.

The results of the coordination parameter measurements using these digitized images together with the algorithm developed in the present work are shown as a function of the packing density Δ in Fig. 4. These results can be compared, for validation, to those directly obtained from the DEM simulations (and thus, giving the exact geometry of the numerical packing).

As shown in Fig. 4(a), the digitization algorithm leads to mean coordination number values that slightly overestimate the DEM computations. Fig. 4(b) indicates that the measured mean contact areas are also somewhat greater than those given by the DEM calculations. This discrepancy is due to the digitization procedure, which artificially increases the measured area somewhat (because of the finite voxel volume), causing for example a nonzero area for a point-contact between two particles. The discrepancy between data from image analysis and simulation is approximately constant and of the order of 0.1 R^2, where R is the particle radius. In what follows, therefore, we correct for this slight discrepancy by imposing this shift to all measured

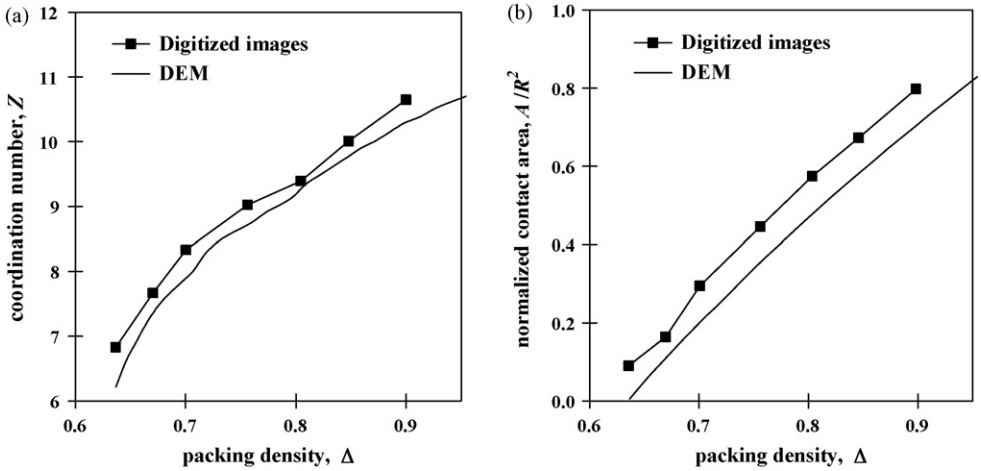

Fig. 4. Comparison of coordination measurements on numerical sphere packings produced by DEM and by analysis of digitized images of these packings using the method developed in the present work: evolution of (a) the mean coordination number Z, and (b) the mean contact area A between touching particles normalized by the square of the particle radius R.

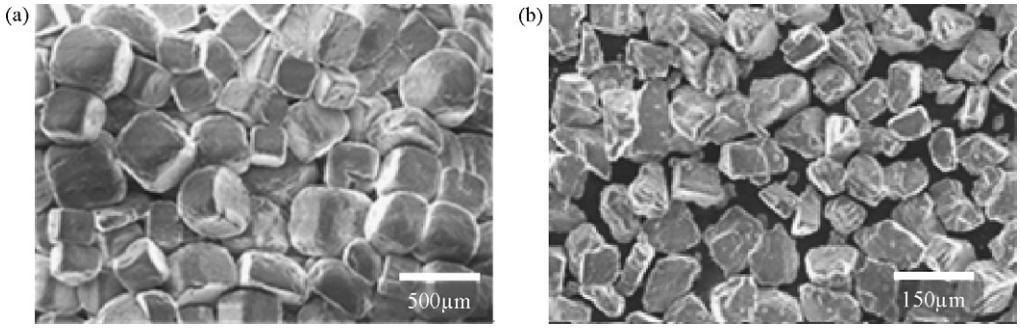

Fig. 5. Scanning electron microscope (SEM) micrographs of as-received NaCl powders used in the present study: (a) coarse particles (400 μm in mean diameter), and (b) fine particles (75 μm in mean diameter).

data so as to correct for the influence of the finite voxel volume; in doing so we implicitly assume that the influence of the contact area shape might have on this slight systematic error of the image analysis routine is negligible.

4. Irregular powders: results and discussion

4.1. Particle characteristics

Table 1 summarizes the values obtained from the 3D image analysis for the two irregular particle types. As seen, these particles are not equiaxed, the 75 μm particles presenting higher aspect ratios than the 400 μm particles. This can also be inferred by observation of particles on scanning electron microscope (SEM) micrographs in Fig. 5. Aspect ratio values furthermore agree with measurements made, also using image analysis of computed X-ray tomography data, on pores of replicated aluminum foams produced from the same salt particles, Table 1 of Ref. 28- which of course is as should be.

The shape of the particles is also visually different, Fig. 5; the 400 μm particles are roughly cubical, whereas the 75 μm particles are more irregular and angular; this difference betrays in all likelihood differences in the way the powders were produced (evaporation tends to produce cubical NaCl crystals, whereas comminution tends to produce more irregular angular particles).

4.2. Particle size distribution

The particle size distribution is obtained using the volume of each separated particle: it is somewhat narrower for the 75 μm than for the 400 μm particles, Fig. 6. The main reason for this is that 75 μm particles have been sieved between 63 and 90 μm meshes, whereas the 400 μm were sieved using only a 250 μm mesh sieve. We note that these size distributions are comparatively narrow: the corresponding standard deviation on the particle diameter is roughly on the order of 20–30% of the average diameter.

Table 1
Mean aspect ratio of the particles indicated by the ratio of principal axis lengths, showing that the present particles have aspect ratios of the type (γ^{-1}, 1, γ)

Particle (μm)	*b*/*a*	*c*/*a*	γ
400	1.22	1.49	1.22
75	1.43	1.97	1.38

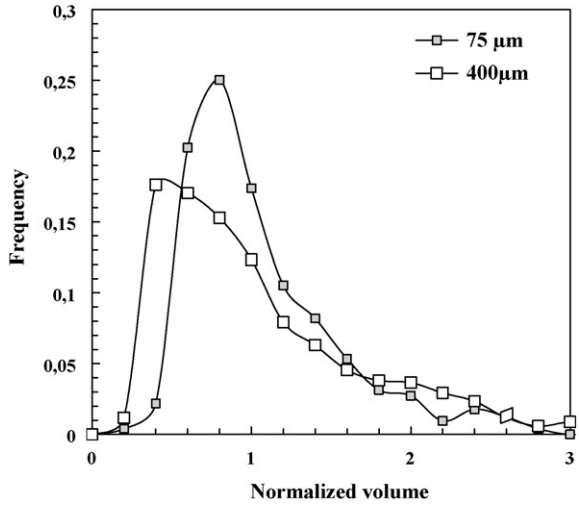

Fig. 6. Size distribution of the salt particles extracted from 3D measurements.

4.3. Initial particle packing

Packing density: Table 2 summarizes the main characteristics of the initial (uncompacted) salt particle packings investigated in the present study. Data include the packing density, the normalized mean contact area between particles A/R^2, and the mean coordination number Z. Packing densities measured from the tomography images (Δ_I) are close to values measured by division of the preform mass by its macroscopic volume (Δ_E), weight-based values being somewhat lower. We refer in what follows to values from image analysis as these pertain to the precise sample volume that was analyzed for Z and A.

Table 2
Initial powder packing characteristics

Particle	Δ_E	Δ_I	A/R^2	Z
400 μm	0.68	0.72	0.4	11.0
75 μm	0.63	0.64	0.12	10.0
Spherical	0.64	0.64	0.0	6.8

Δ_E is the weighted density, Δ_I density measured by image analysis, A/R^2 the initial particle contact area A normalized by the square of the particle radius R, and Z the initial coordination number.

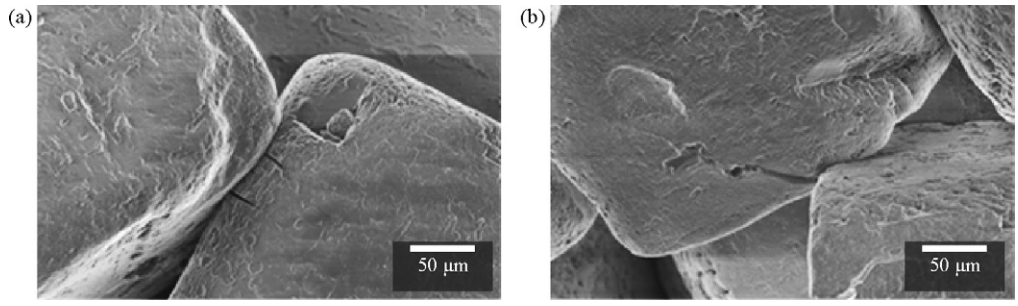

Fig. 7. SEM micrographs of 400 μm salt particles compacted at 28 MPa. Thin cracks are noticeable at contact points between the particles.

Table 2 indicates that the initial packing densities differ somewhat between the two powders. The 75 μm powder exhibits an initial packing density similar to that of dense random packing of monomodal spheres (0.64). The 400 μm powder packs to a higher initial relative density (0.72).

The higher initial packing density of the 400 μm powder can be explained by several factors, namely the somewhat greater spread in particle size distribution (Fig. 6) and the particle shape.

An increase in particle size distribution generally (but not always) causes, all else equal, an increase in powder packing density .[4,21,35–40] With a standard deviation in particle diameters on the order of 30% of the average particle diameter, comparison with simulation or experimental data in Refs. 4,35,36,41 for the initial packing of continuously distributed particles indicates that this effect could account for an increase in packing density on the order of only a few percent; hence, the spread in particle size can only explain part of the observed higher packing density of the 400 μm particles over monosized spheres or the 75 μm particles. That size distribution effects are not chiefly responsible for the higher initial packing density of the 400 μm powder versus the 75 μm powder also agrees with the observation that, if these two distributed powders are made spherical by melting in a propane torch as described in Ref. 42, they pack to the same density (near 65%; determined by weight and hence influenced by solidification shrinkage porosity within the rounded NaCl particles).[43]

This would thus lead to conclude that it is mainly the shape of the 400 μm particles that causes them to pack to higher initial densities than the 75 μm particles (or monosized spheres). Generally, a departure from sphericity is found to cause a decrease in initial packing density of spheres or powders[4,21,44]; however, there are simulation results and experimental data showing that the opposite effect, of increased packing density with decreasing sphericity, can be found with limited departures from a sphere, particularly if powders are tapped when packed.[4,21,23–25] Table 1 shows that the aspect ratio of the present salt particles is not far from being of the type (γ^{-1}, 1, γ) that was simulated in Refs. 23,24 Using the data in Fig. 1 of Ref. 24, one finds that the packing density Δ should be near 0.73 for both $\gamma = 1.22$ and 1.38: this value in fact agrees well with that measured here for the coarser, 400 μm particles. That it does not for the 75 μm particles may be caused by their greater roughness and angularity, Fig. 5 (an extreme analogy with "hairy" particles makes the effect clear).

Coordination: Table 2 shows that the average coordination number Z of the initial packing for both kinds of particles ($Z = 10$ and $Z = 11$) is significantly larger than for spherical particles (typically $Z = 6$ for random close packed spheres[1,12–14,23,24]). This observation is not likely to be caused by the spread in particle size. There is indeed ample evidence, both theoretical and experimental,[4,18,45–49] that packings of spheres exhibiting both discrete or continuous distributions in their size maintain the same *average* coordination number $Z = 6$ characteristic of monosized sphere packings. That the initial value of average coordination with the salt particles is significantly above six is therefore to be attributed to their shape. This is in agreement with data and simulations in Refs. 23,24, which show that Z exhibits a cusp at $\gamma = 1$ (i.e., for spheres). The values measured with the present irregular particles are indeed relatively close to values calculated by Chaikin et al.[24], namely $Z = 11.5$ and 10, for $\gamma = 1.38$ and 1.22 (Table 1), respectively. A similar effect, of increased coordination with departure from sphericity of packed near-spheroidal particles is also documented in Ref. 25.

4.4. Cold-compacted powders

Figs. 7 and 8 give close-ups of particle/particle contact points after cold compaction. These micrographs show that the NaCl particles densify during cold compaction by a combination of plastic deformation (also visible in Fig. 7(f) of Ref. 42), with occasional particle fracture (illustrated in Fig. 8).

Fig. 9 presents the influence of packing density on the coordination number Z of powders that have been isostatically cold-compacted above their tap density. Several conclusions can be drawn from these data: (i) there is no discernible difference

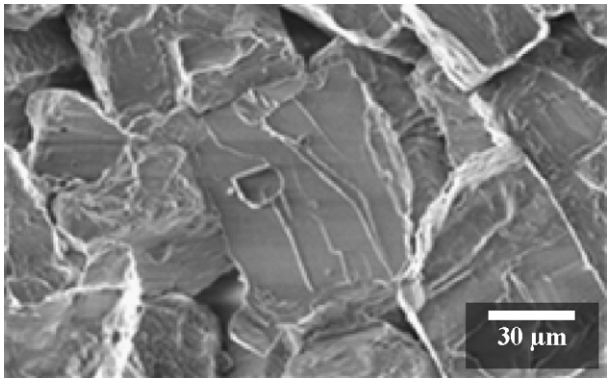

Fig. 8. SEM micrograph of 75 μm salt particles compacted at 46 MPa, showing an instance of a fully fractured particle.

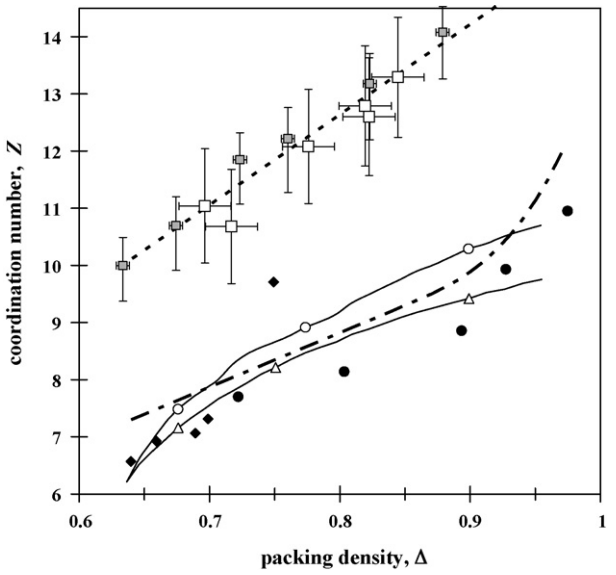

Fig. 9. Evolution of the mean coordination number Z with packing density: experimental data from the present study 75 (▩) and 400 μm salt (□) and linear fit (- - - -), compared with experimental data of isostatic compaction of sphere packings from Fischmeister et al.[8] (●) and Uri et al. [12] (⧫), predictions from the discrete element simulations of this work without friction (◯) and with friction $\mu = 0.2$ + no particle rotation (△), and analytical sphere packing model of Arzt for cold-compaction (— - —)[1].

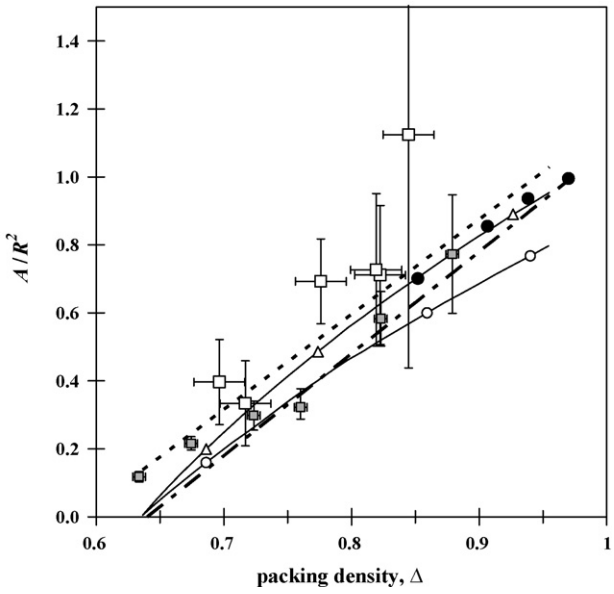

Fig. 10. Evolution of the mean interparticle contact area A normalized by the square of the particle radius R with packing density: experimental data from the present study 75 (▩) and 400 μm salt (□) and linear fit (- - - -), compared with experimental data from Fischmeister et al.[8] (●), predictions from the discrete element simulations of this work without friction (◯) and with friction $\mu = 0.2$ + no particle rotation (△), and analytical sphere packing model of Arzt for cold-compaction (— - —) [1].

between the 75 and the 400 μm particles within the scatter of experimental data (despite their different initial packing densities), and (ii) the coordination number Z is approximately proportional to the powder compact density: the dotted line through the data in Fig. 9 corresponds to $Z = 15.8\ \Delta$. Comparing this line with the two curves for simulated sphere packings DEM, and with the Arzt model prediction for particle compaction (which as seen shows good agreement with the simulations, particularly with an interparticle friction coefficient $\mu = 0.2$ and no particle rotation), these compacted irregularly shaped packed particles have roughly 50% more mutual contact points than spheres. The fact that the two data sets superimpose despite the difference in initial packing density reinforces the suggestion that the initial difference is due to angularity and roughness along the surface of the 75 μm particles: after compaction, sharp angles and roughness are simply erased at particle contact regions.

Fig. 10 plots the average particle contact area A normalized by the square of the average particle radius R. Inspection of Fig. 10 shows that the initial contact area is not zero for both particle types: A/R^2 is equal to 0.12 for the 0.75 μm particles and 0.4 for the 400 μm particles. This indicates that at least some of the contacts between the uncompressed particles are not point contacts. This observation has a simple explanation: parallel particle facets touch spontaneously along a finite surface area. An example of such a contact can be seen in Fig. 11.

As was found for Z, the two data sets for A/R^2 are close: the 400 μm particle data suggest a somewhat higher rate of increase for A with increasing packing density than the 75 μm particles but the difference remains within the experimental uncertainty. The data furthermore superimpose well with the curve for simulated DEM sphere packings for realistic interparticle friction ($\mu = 0.2$) and no particle rotation (justified by the large size of the plastic contacts), and also with the Arzt model prediction. Thus, despite (i) the different initial packing density, (ii) the clearly non-spherical shape of the particles (Figs. 2, 5 and 11), and (iii) a 50% higher coordination number Z, these irregular particles show a normalized interparticle contact area that is, for all practical purposes, the same as that of spherical particles packed to the same relative density. The only significant difference lies in

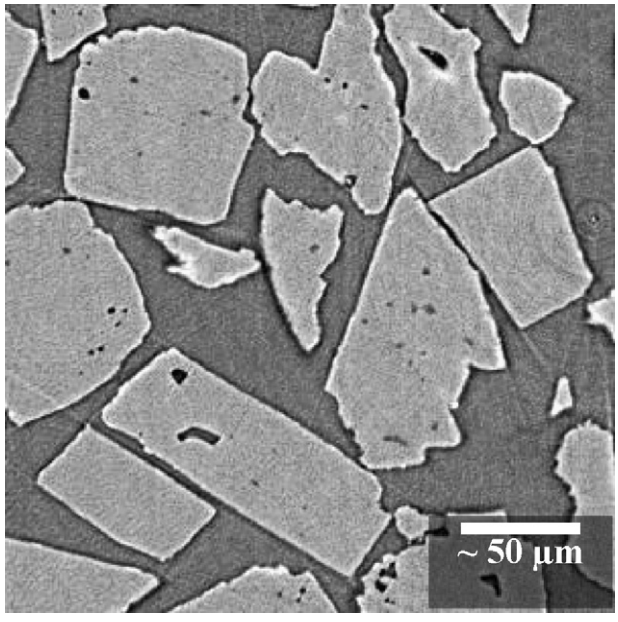

Fig. 11. Large contact areas between flat facets of touching particles within the as-packed (non-compacted) 75 μm particle bed.

the initial value. As with Z, here too the present data can be described by a simple linear fit:

$$\frac{A}{R^2} = 2.8(\Delta - \Delta_0) + \left(\frac{A}{R^2}\right)_0 \quad (1)$$

where $(A/R^2)_0 = 0.12$ and $\Delta_0 = 0.63$. The fact that A is approximately the same for angular and spherical particles has implications since some properties of porous materials are dominated by this parameter.

One such property is the permeability to viscous fluid flow through open-pore metal foams produced by infiltration of such NaCl preforms. It was shown in Ref. 50 that this important property of open-pore foams can quite accurately be predicted knowing the size of windows between pores in the metal foam, equal in replicated foams to the contact area A in the salt particle preform from which the foam was made. Experiment shows that foams made from spherical and from irregular NaCl particles of identical size have very similar permeabilities, see Fig. 4 of Ref. 50 This observation is consistent with the fact that (A/R^2) is identical for both particle types.

The rate of densification of the powder compacts is also governed by the relative size of interparticle necks. Sphere-based models of densification furthermore show that the rate of preform densification (for time-dependent processes) or the extent of densification (for time-independent processes such as cold-compaction) at given Δ is a relatively weak function of Z[1,3,10] while it depends strongly on the instantaneous value of A/R^2. The present results show that the difference in Z between packed spheres and irregular particles is on the order of 50% while the relative size of interparticle necks (A/R^2) is essentially the same. Given the uncertainty that exists in many of the parameters that govern densification (these include surface energies, diffusion constants or creep laws), the error introduced in applying densification laws derived for spheres to angular particle preforms should therefore, be quite small.

The present data thus help explain why models derived for Stage I densification of monomodal spherical particles have good predictive power even when applied to the densification of clearly non-spherical particle preforms.[1–3,51]

5. Conclusion

3D image analysis methods are developed to measure the evolution of particle coordination and average contact area during the cold-compaction of irregular NaCl powder particles. These methods are validated using digitized numerical sphere packings produced by the DEM.

It is shown that initial packings of the irregular salt particles display (i) a higher initial coordination number than spheres, and (ii) a somewhat variable initial packing fraction. These effects can at least in part be ascribed to the non-unity aspect ratio of the particles, with a possible additional effect on the initial packing density of particle surface roughness and of the finite spread in particle size. Uncompacted NaCl powder preforms also show a finite average particle contact area; this is explained by mutual contact of flat facets on the virgin particles.

Data for the average coordination number and average normalized contact area of cold isostatically compacted preforms plotted as a function of relative density superimpose approximately despite the difference in shape of the two types of particle explored here. The average coordination number of irregular particles remains higher than for spheres, by roughly 50% over the entire range explored, and varies proportionally with the relative density. The average contact area between cold-compacted irregular particles on the other hand superimposes on both data and model predictions for spherical particles over the entire range explored. It should be clear that the present results are limited to one particular type of irregular particles (cuboid-like) and that Eq. (1) may not hold for other morphologies in its present simplistic form. Also, the fact that the powders were vibrated before compaction is likely to have influenced the geometric configuration of the packing. Rotations and particle rearrangements, triggered by vibrations, may explain in part the high initial coordination number observed with irregular particles packings; further research would be needed to quantify the effect. Finally we note that the observation that the contact area is not affected strongly by particle shape in the present preforms suggests that models derived assuming monomodal spheres are good predictors for their densification, even though these particles are clearly not spherical.

6. Summary of conclusions

The present observations show that models derived assuming monomodal spheres can be good predictors for the densification of powders even when particles are clearly not spherical.

Acknowledgements

This work was supported by the French Ministère de l'Education Nationale de la Recherche et de la Technologie. We thank Mr. Jean Michel Missiaen for his help on image analysis. Great thanks are also due to Ms. Elodie Boller, local contact at ID 19 for her availability. The work at EPFL was funded by the Swiss National Science Foundation, Project No. 200020-100179/1.

References

1. Arzt, E., The influence of an increasing particle coordination on the densification of spherical powders. *Acta Metall.*, 1982, **30**, 1883–1890.
2. Arzt, E., Ashby, M. F. and Easterling, K. E., Practical applications of hot-isostatic pressing diagrams: four case studies. *Metall. Trans.*, 1983, **14A**, 211.
3. Ashby, M. F., In *Sintering and Hot Isostatic Pressing Diagrams Powder Metallurgy: An Overview*, ed. I. Jenkins and J. V. Wood. The Institute of Metals, London, UK, 1991, p. 144.
4. German, R. M., *Particle Packing Characteristics Metal Powder Industries*. Federation, Princeton, 1989, 443 p.
5. German, R. M., *Sintering Theory and Practice*. John Wiley & Sons, New York, 1996, 550 p.
6. Evans, J. W. and DeJonghe, L. C., *The Production of Inorganic Materials*. Macmillan Publishing Company, New York, 1991, 541 p.
7. Reed, J. S., *Principles of Ceramics Processing* (*2nd ed.*). J. Wiley & Sons, New York USA, 1995, 658 p.

8. Fischmeister, H. F., Artz, E. and Olsson, L. R., Particle deformation and sliding during compaction of spherical powders: a study by quantitative metallography. *Powder Metall.*, 1978, **21**, 179–187.
9. Fischmeister, H. F. and Artz, E., Densification of powders by particle deformation. *Powder Metall.*, 1983, **26**, 82–88.
10. Helle, A. S., Easterling, K. E. and Ashby, M. F., Hot-isostatic pressing diagrams: new developments. *Acta Metall.*, 1985, **33**, 2163.
11. Fleck, N. A., On the cold compaction of powders. *J. Mech. Phys. Solids*, 1995, **43**, 1409–1431.
12. Uri, L., Walmann, T., Alberts, A., Dysthe, D. K. and Feder, J., Structure of plastically compacting granular packings. *Phys. Rev. E*, 2006, **73**, 051301.
13. Heyliger, P. R. and McMeeking, R. M., Cold plastic compaction of powders by a network model. *J. Mech. Phys. Solids*, 2001, **49**, 2031–2054.
14. Martin, C. L., Bouvard, D. and Shima, S., Study of particle rearrangement during powder compaction by the discrete element method. *J. Mech. Phys. Solids*, 2003, **51**, 667–693.
15. Martin, C. L., Delette, G. and Bouvard, D., Compaction of ceramic aggregated powders. *J. Am. Ceram. Soc.*, 2006, **89**, 3379–3387.
16. Seidler, G. T., Martinez, G., Seeley, L. H., Kim, K. H., Behne, E. A., Zaranek, S., Chapman, B. D., Heald, S. M. and Brewe, D. L., Granule-by-granule reconstruction of a sandpile from X-ray microtomography data. *Phys. Rev. E*, 2000, **62**, 8175–8181.
17. Aste, T., Saadatfar, M. and Senden, T. J., Geometrical structure of disordered sphere packings. *Phys. Rev. E*, 2005, **71**, 061302.
18. Georgalli, G. A. and Reuter, M. A., Modelling the co-ordination number of a packed bed of spheres with distributed sizes using a CT scanner. *Minerals Eng.*, 2006, **19**, 246–255.
19. Atwood, R. C., Jones, J. R., Lee, P. D. and Hench, L. L., Analysis of pore interconnectivity in bioactive glass foams using X-ray microtomography. *Scripta Mater.*, 2004, **51**, 1029–1033.
20. Vagnon, A., Riviere, J. P., Missiaen, J. M., Bellet, D., Di Michiel, M., Josserond, C. and Bouvard, D., X-ray microtomography analysis of the evolution of 3D microstructural characteristics during sintering of a copper powder. In *Proceedings of the Powder Metallurgy World Congress, Vienna, 2004 EPMA, Vol. 5*, 2006. p. 415–422.
21. Cumberland, D. J. and Crawford, R. J., *The Packing of Particles*. Elsevier, Amsterdam, 1987, p. 103–105.
22. Peronius, N. and Sweeting, T. J., On the correlation of minimum porosity with particle size distribution. *Powder Technol.*, 1985, **42**, 113–121.
23. Donev, A., Cisse, I., Sachs, D., Variano, E. A., Stillinger, F. H., Connelly, R., Torquato, S. and Chaikin, P. M., Improving the density of jammed disordered packings using ellipsoids. *Science*, 2004, **303**, 990–993.
24. Chaikin, P. M., Donev, A., Man, W., Stillinger, F. H. and Torquato, S., Some observations on the random packing of hard ellipsoids. *Ind. Eng. Chem. Res.*, 2006, **45**, 6960–6965.
25. Hopkins, M. A., Discrete element modeling with dilated particles. *Eng. Comput.*, 2004, **21**, 422–430.
26. Favier, J. F., Abbaspour-Fard, H. H. and Kremmer, M., Modeling nonspherical particles using multisphere discrete elements. *J. Eng. Mech.*, 2001, **127**, 971–977.
27. Smith, L. N. and Midha, P. S., Computer simulation of morphology and packing behaviour of irregular particles, for predicting apparent powder densities. *Comput. Mater. Sci.*, 1997, **7**, 377–383.
28. San Marchi, C. and Mortensen, A., Infiltration and the replication process for producing metal sponges. In *Handbook of Cellular Materials—Production, Processing Applications*, ed. H. P. Degischer. Wiley–VCH, Weinheim, 2002, p. 44 [chapter 2.6].
29. Conde, Y., Despois, J.-F., Goodall, R., Marmottant, A., Salvo, L., Marchi, C. S. and Mortensen, A., Replication processing of highly porous materials. *Adv. Eng. Mater.*, 2006, **8**, 795.
30. Thompson, K. E., Willson, C. S. and Zhang, W. L., Quantitative computer reconstruction of particulate materials from microtomography images. *Powder Technol.*, 2006, **163**, 169–182.
31. Fu, X. W., Dutt, M., Bentham, A. C., Hancock, B. C., Cameron, R. E. and Elliott, J. A., Investigation of particle packing in model pharmaceutical powders using X-ray microtomography and discrete element method. *Powder Technol.*, 2006, **167**, 134–140.
32. Sweeney, S. M. and Martin, C. L., Pore size distributions calculated from 3-D images of DEM-simulated powder compacts. *Acta Mater.*, 2003, **51**, 3635.
33. Beucher, S. and Lantuéjoul, C., Use of watersheds in contour detection. In *Proceedings of the International Workshop on Image Processing, Real-time Edge and Motion Detection/Estimation*, 1979.
34. Lorensen, W. and Harvey, E. C., Marching cubes: a high-resolution 3D surface construction algorithm. In *Proceedings of the SIGGRAPH 87, Computer Graphics, 21 July (4)*, 1987. p. 163–170.
35. Ma, J. and Lim, L. C., Effect of particle size distribution on sintering of agglomerate-free submicron alumina powder compacts. *J. Eur. Ceram. Soc.*, 2002, **22**(13), 2197.
36. Bierwagen, G. P. and Sanders, T. E., Studies of the effects of particle size distribution on the packing efficiency of particles. *Powder Technol.*, 1974, **10**, 111–119.
37. Suzuki, M. *et al.*, Effect of size distribution on tapping properties of fine powder. *Powder Technol.*, 2001, **118**, 53–57.
38. Yu, A. B. and Standish, N., Porosity calculations of ternary mixtures of spherical particles. *Powder Technol.*, 1987, **52**, 249–253.
39. Yu, A. B. and Standish, N., Porosity calculations of multi-component mixtures of spherical particles. *Powder Technol.*, 1987, **52**, 233–241.
40. Yu, A. B. and Standish, N., An analytical–parametric theory of the random packing of particles. *Powder Technol.*, 1988, **55**, 171–186.
41. Cumberland, D. J., Crawford, R. J. and Sprevak, D., A statistical model for the random packing of real powder particles. *Eur. Polym. J.*, 1989, **25**, 1173.
42. Goodall, R., Marmottant, A., Salvo, L. and Mortensen, A., *Mater. Sci. Eng. A*, 2007, **465**, 124.
43. Marmottant, A., Structure et propriétés de mousses d'aluminium élaborées par réplication de préformes de sel. Doctoral Thesis. Institut National Polytechnique de Grenoble: Grenoble, France, 2006, p.III-5.
44. Yu, A. B. and Standish, N., Characterisation of non-spherical particles from their packing behaviour. *Powder Technol.*, 1993, **74**, 205–213.
45. Suzuki, M. and Oshima, T., Estimation of the co-ordination number in a multi-component mixture of cohesive spheres. *Powder Technol.*, 1983, **36**, 159–166.
46. Suzuki, M. and Oshima, T., Estimation of the co-ordination number in a two-component mixture of cohesive spheres. *Powder Technol.*, 1983, **36**, 181–188.
47. Suzuki, M. and Oshima, T., Co-ordination number of a multi-component randomly packed bed of spheres with size distribution. *Powder Technol.*, 1985, **44**, 213–218.
48. Suzuki, M. and Oshima, T., Comparison between the computer-simulated results and the model for estimating the co-ordination number in a three-component random mixture of spheres. *Powder Technol.*, 1985, **44**, 19–25.
49. Pinson, D., Zou, R. P., Yu, A. B., Zulli, P. and McCarthy, M. J., Coordination number of binary mixtures of spheres. *J. Phys. D: Appl. Phys.*, 1998, **31**, 457–462.
50. Despois, J. F. and Mortensen, A., Permeability of open-pore microcellular materials. *Acta Mater.*, 2005, **53**, 1381–1388.
51. Goodall, R., Despois, J. F. and Mortensen, A., Sintering of NaCl powder: mechanisms and first stage kinetics. *J. Eur. Ceram. Soc.*, 2006, **26**, 3487–3497.